Journal of
Materials Chemistry A

PAPER

View Article Online
View Journal | View Issue

Cite this: *J. Mater. Chem. A*, 2025, **13**, 17944

Room-temperature barocaloric effect in [Fe(pap-$5NO_2)_2$] spin-crossover material†

David Gracia, *[ab] Vera Cuartero, [ac] Catalin Popescu, [d] Adelais Trapali, [e] Talal Mallah, [e] Marie-Laure Boillot, [e] Javier Blasco, [ab] Gloria Subías [ab] and Marco Evangelisti [ab]

Received 2nd January 2025
Accepted 12th May 2025

DOI: 10.1039/d5ta00033e

rsc.li/materials-a

We examine the pressure dependence of the spin-crossover transition in [Fe(pap-$5NO_2)_2$] that occurs near room temperature. We employ a combination of high-pressure calorimetry and powder X-ray diffraction measurements, conducted both under variable-pressure and variable-temperature conditions. Both methods indicate that the spin-crossover transition shifts linearly to higher temperatures with increasing pressure, while simultaneously exhibiting an increase in the width of the thermal hysteresis. We report a giant barocaloric effect, revealing isothermal entropy changes in the 70–79 J kg^{-1} K^{-1} range and adiabatic temperature changes between 20 and 26 K for a pressure change of 2.0 kbar. Although the effect diminishes under reversible conditions, it remains substantial, with values of 70 J kg^{-1} K^{-1} and 14 K, respectively.

1 Introduction

Solid-state refrigeration is emerging as a promising alternative to traditional refrigeration systems that operate on the compression and expansion of greenhouse gases.[1,2] This technology is based on the principle of the caloric effects, which refer to the reversible thermal changes in isothermal entropy, ΔS_T, and adiabatic temperature, ΔT_{ad}, following the application (or removal) of an external field. In particular, the BaroCaloric Effect (BCE) allows certain materials to respond to changes in the hydrostatic pressure, Δp. Recently, near-room-temperature barocaloric refrigeration has gained significant attention, primarily due to the observation of larger values of ΔS_T and ΔT_{ad} than those found in other caloric materials.[3–5] For scalable barocaloric refrigeration to become a reality, it is crucial to identify materials that undergo first-order solid–solid phase transitions that are highly sensitive to pressure, while being accompanied by high entropy and volume changes. Furthermore, maintaining a low thermal hysteresis ensures optimal performance during pressure cycling.[6]

Spin-CrossOver (SCO) compounds have been identified as excellent barocaloric materials.[7] SCO transitions typically occur in octahedrally coordinated Fe^{II} complexes with a $3d^6$ electronic configuration. These transitions involve a shift between a diamagnetic Low-Spin (LS, $s = 0$) state and a paramagnetic High-Spin (HS, $s = 2$) state.[8,9] A notable characteristic of these transitions is the large unit-cell volume change that arises due to the reversible shortening (lengthening) of the Fe^{II} bond lengths during the SCO process.[10] This property makes SCO transitions particularly sensitive to changes in pressure.[11] In recent years, large BCE responses have been predicted to take place at the SCO transition temperature of various Fe^{II} compounds.[12–15] However, only a limited number of SCO compounds have been thoroughly explored using high-pressure calorimetry techniques.[16–20]

Here, we focus on the Fe^{II} Schiff-base SCO compound [Fe(pap-$5NO_2)_2$] (Fig. 1), with chemical formula $C_{24}H_{16}FeN_6O_6$, where the

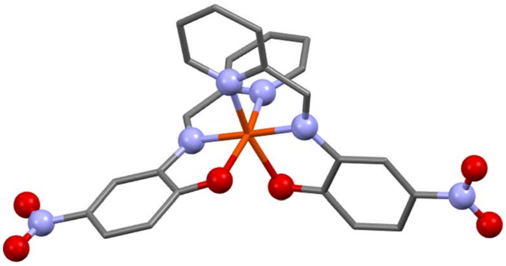

Fig. 1 View of the molecular structure of [Fe(pap-$5NO_2)_2$], (oxygen atoms, red; nitrogen atoms, blue), H atoms were removed for clarity.

---

[a] Instituto de Nanociencia y Materiales de Aragón (INMA), CSIC-Universidad de Zaragoza, 50009 Zaragoza, Spain. E-mail: davidg@unizar.es

[b] Departamento de Física de la Materia Condensada, Universidad de Zaragoza, Calle Pedro Cerbuna 12, 50009 Zaragoza, Spain

[c] Departamento de Ciencia y Tecnología de Materiales y Fluidos, EINA, Universidad de Zaragoza, Calle María de Luna 3, 50018 Zaragoza, Spain

[d] CELLS – ALBA Synchrotron, 08290 Cerdanyola del Valles, Barcelona, Spain

[e] Institut de Chimie Moléculaire et des Matériaux d'Orsay, CNRS UMR 8182, Université Paris-Saclay, 17, avenue des Sciences, 91400 Orsay, France

† Electronic supplementary information (ESI) available: XRPD patterns (Fig. S1); magnetic properties with and without Apiezon H (Fig. S2); pressure dependence of HS and LS molar fractions (Fig. S3); pressure dependence of unit-cell parameters (Fig. S4); isobaric thermograms for multiple thermal cycles (Fig. S5). See DOI: **https://doi.org/10.1039/d5ta00033e**

ligand Hpap-5NO$_2$ is the condensation product of pyridine-2-carbaldehyde with 2-hydroxy-5-nitroaniline. As previously reported,[21] [Fe(pap-5NO$_2$)$_2$] showcases a highly cooperative first-order SCO transition that occurs around room temperature. This transition is marked by a significant volume change occurring between two isostructural monoclinic phases (space group *C*2/*c*). Upon heating, the monoclinic unit cell undergoes an abrupt expansion of the *b* axis coupled to a shrinkage of the *a* axis, and an increase of the monoclinic distortion. Differential Scanning Calorimetry (DSC) measurements conducted at ambient pressure have estimated a total entropy change of $\Delta S_{\mathrm{SCO}} \approx 56$ J kg^{-1} K^{-1} during the SCO transition. In this work, we utilize high-pressure calorimetry and Synchrotron X-ray Powder Diffraction (SXRPD) measurements to investigate the pressure dependence of the thermal and structural properties throughout the SCO transition in [Fe(pap-5NO$_2$)$_2$]. The SXRPD experiments are performed under isothermal and variable-pressure conditions. Additionally, X-ray Powder Diffraction (XRPD) patterns are collected at our home laboratory under variable temperature and ambient-pressure conditions. Using calorimetric and structural data, we have identified a remarkably large BCE near ambient temperature in [Fe(pap-5NO$_2$)$_2$].

2 Materials and methods

The polycrystalline [Fe(pap-5NO$_2$)$_2$] powder sample was prepared under dry and anaerobic conditions by an experimental procedure based on a previously employed route.[21] Specifically, Hpap-5NO$_2$ (129 mg, 0.53 mmol) was dissolved in 30 mL of a DCM/MeOH (1 : 2 v/v) solution containing 73.9 μL of Et$_3$N (53.6 mg, 0.53 mmol). The obtained mixture was layered with 10 mL of MeOH, to which 10 mL of FeBF$_4\cdot$6H$_2$O (89.5 mg, 0.265 mmol) methanolic solution was carefully placed on top. [Fe(pap-5NO$_2$)$_2$] was obtained as needle-like violet crystals within approximately 10 days, which were carefully collected *via* cannula filtration and further washed with aliquots of MeOH (63 mg, 44%). The resulting powder was checked with XRPD measurements (Fig. S1†), using a Philips PANalytical X'Pert Pro MPD diffractometer at Cu Kα radiation, equipped with a fast detector within the 5–43° 2θ range. A soft grinding was applied to the dry samples to homogenize and reduce the grain size.

Variable-pressure isothermal SXRPD measurements were conducted at the Materials Science and Powder Diffraction (MSPD) beamline of the ALBA synchrotron.[22] Polycrystalline sample was dispersed in Daphne oil 7373 and loaded in a membrane-free diamond anvil cell for the experiments. We used Daphne oil 7373 as the pressure transmitting medium because above room temperature it remains hydrostatic up to ~22 kbar.[23] Pressure was determined using the NaCl equation of state.[24] The sample temperature was controlled by a combination of a resistive heater and a K-type thermocouple. Data were collected across the pressure range from 0 to 6 kbar along with three distinct isotherms ranging from 310 to 330 K, using a monochromatic beam with wavelength 0.4246 Å and a spot size of 15 μm × 15 μm at full width at half-maximum. For each isotherm, fresh sample was loaded in the membrane-free diamond anvil cell. A SX165 Rayonix MarCCD detector was used to collect the diffraction patterns. They were measured in the angular 2θ range from 2° to 14°, and integrated into conventional X-ray diffraction patterns using the software DIOPTAS.[25] Additionally, variable-temperature isobaric XRPD characterization at ambient pressure was performed, covering the temperature range from 220 to 370 K with a Rigaku D-Max system using Cu K$\alpha_{1,2}$ wavelengths. Le Bail refinements were executed using the Fullprof program,[26] with refined parameters including the 2θ offset and unit-cell parameters to assess volume changes between the LS and HS phases.

High-pressure calorimetry experiments were carried out using a custom-built calorimeter implemented inside a piston-cylinder CuBe high-pressure cell. A Surface Mount Device (SMD) resistor of 1 kΩ (±1% tolerance) was utilized both as sample-holder and pressure sensor, while Daphne oil 7373 served as the hydrostatic pressure-transmitting medium. The entire system was housed in a liquid-nitrogen-based cryostat, Oxford Instruments Optistat$^{\mathrm{DN}}$, which operates within the temperature range from 77 to 400 K. The sample, in powder form, was mixed in a 50–50% ratio with Apiezon H grease to create a slurry weighing a few milligrams. Magnetization measurements, collected with a Quantum Design PPMS DynaCool equipped with the vibrating sample magnetometer option, discarded adverse effects on [Fe(pap-5NO$_2$)$_2$] from the use of Apiezon H (Fig. S2†). The temperature dependence of the isobaric heat capacity at various pressures was derived from continuously recording the temperature of the sample with a K-type thermocouple (±0.75% accuracy) in contact with the sample, complemented by a Pt100 sensor (class A with ±0.15 K tolerance) positioned outside the pressure cell. These sets of data, hereafter denoted as thermograms,[27] were collected in arbitrary units during heating and cooling ramps of ±5 K min^{-1}. Absolute values were obtained by calibrating the ambient-pressure data with previously reported DSC measurements with a TA Instruments Q-20a.[21] An indirect estimation of ΔS_{T} and ΔT_{ad} was performed in accordance with standard thermodynamic formulations.[28]

3 Results and discussion

3.1 X-ray powder diffraction at ambient pressure

As anticipated, [Fe(pap-5NO$_2$)$_2$] undergoes a thermally induced transition between the LS and HS phases as it approaches approximately 300 K at ambient pressure.[21] Fig. 2 shows examples of XRPD patterns collected before and after the SCO transition. The monoclinic *C*2/*c* structure is preserved upon heating. At the SCO transition temperature, we observe a notable isobaric volume change of $\Delta V_{\mathrm{p}} = 48 \pm 4$ Å^3 for $Z = 4$ (Fig. 3), which corresponds to 2.3% of the total volume. The volume thermal expansion coefficient, defined as

$$\beta = \frac{1}{V}\left(\frac{\mathrm{d}V}{\mathrm{d}T}\right)_p, \qquad (1)$$

is calculated close to the SCO transition, yielding values of $\beta = (1.6 \pm 0.1) \times 10^{-4}$ K^{-1} for the LS phase and $\beta = (0.7 \pm 0.1) \times 10^{-4}$ K^{-1} for the HS phase.

Assuming that at the SCO transition temperature the transformation from spin states $s = 0$ to $s = 2$ is fully realized, the

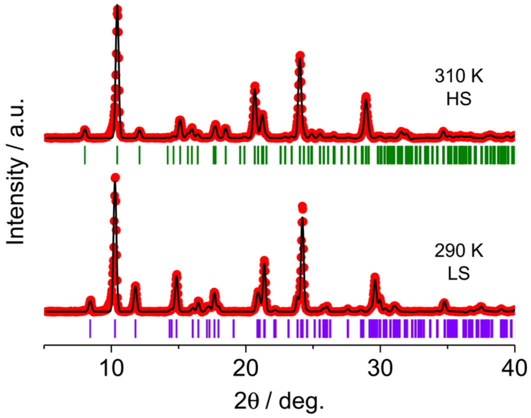

Fig. 2 XRPD patterns collected at ambient pressure at two selected temperatures, for [Fe(pap-5NO$_2$)$_2$]. The red symbols correspond to the experimental data and the black solid lines to the Le Bail refinements. The allowed reflections for the HS and LS phases are depicted in green and purple, respectively.

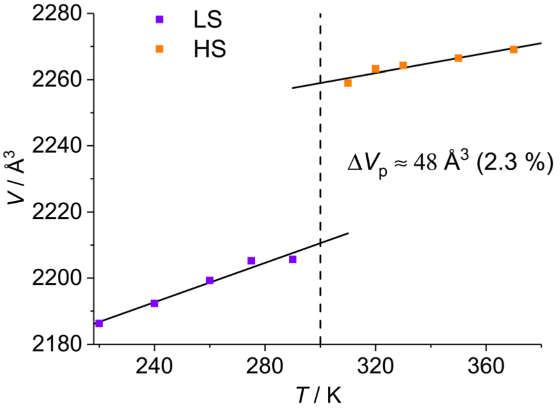

Fig. 3 Thermal expansion at ambient pressure for [Fe(pap-5NO$_2$)$_2$]. The solid lines are fits to the data, and the vertical dashed line indicates the approximate transition temperature. The standard deviations are smaller than the symbols sizes.

magnetic entropy change is given by $\Delta S_m = R\ln(2s + 1) = 25$ J kg^{-1} K^{-1}.[21] Therefore, the remaining entropy (~30 J kg^{-1} K^{-1}) up to the total entropy change at the SCO transition, determined from DSC measurements,[21] must be attributed to the entropy change associated with crystal lattice vibrations and molecular distortions. This contribution is estimated as

$$\Delta S_v = \left(\frac{\bar{\beta}}{\bar{\kappa}}\right)\Delta V_p, \qquad (2)$$

where $\bar{\beta}$ and $\bar{\kappa}$ represent the average thermal expansion and isothermal compressibility near the SCO transition, respectively.[29] To determine $\bar{\kappa}$, we have investigated the pressure dependence of the SCO transition by SXRPD measurements.

3.2 Synchrotron powder X-ray diffraction at variable pressure

The isothermal variable-pressure SXRPD measurements were conducted alongside three isotherms at 310, 320 and 330 K. At ambient pressure, for each isotherm, [Fe(pap-5NO$_2$)$_2$] exhibited characteristics consistent with its pure HS phase. As the pressure was increased, the SCO transition to the LS phase was induced. This behavior is depicted in Fig. 4 for the isotherm recorded at 320 K, as a matter of illustration. As can be seen, a change of pressure of ~1.5 kbar under compression, namely from 1.7 to 3.2 kbar, induces a complete transformation between the HS and LS states. Conversely, a similar but reversed change of ~1.3 kbar under decompression, from 1.4 to 0.1 kbar, drives the complete transformation from LS to HS states.

To evaluate the pressure hysteresis, we display the isothermal pressure–volume, p–V, dependence of [Fe(pap-5NO$_2$)$_2$] at the three measured temperatures during both compression and decompression in Fig. 5(a–c). Volume data are presented only when the material is in a single phase due to the uncertainty associated with extracting reliable unit-cell parameters from the powder patterns within the phase coexistence region. Nevertheless, we could approximately determine the molar fraction of each phase when a coexistence of HS and LS phases was identified, as illustrated in Fig. 5(d) for 320 K (see Fig. S3† for the molar fraction plots at 310 and 330 K). As clearly seen, the pressure required to trigger the transition rises with increasing temperature, accompanied by a notable pressure hysteresis. The variations of the lattice parameters during the $s = 2$ to $s = 0$ transformation under pressure are qualitatively like those of the SCO thermal process (Fig. S4†).[21]

The isothermal compressibility has been calculated as

$$\kappa = -\frac{1}{V}\left(\frac{\mathrm{d}V}{\mathrm{d}p}\right)_T, \qquad (3)$$

yielding values ranging from 5×10^{-3} to 8×10^{-3} kbar^{-1}, which is relatively low when compared with other SCO

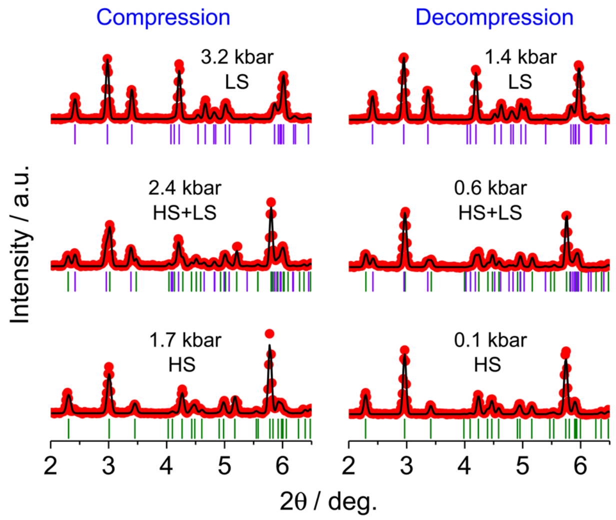

Fig. 4 SXRPD patterns of [Fe(pap-5NO$_2$)$_2$], collected at $T = 320$ K at three different values of pressure under compression (left) and decompression (right), as indicated, for a selected angular range. The red circles correspond to the experimental data, while the black solid lines are the Le Bail refinements. The structures are indicated, and so are the allowed reflections for the HS and LS phases in green and purple, respectively.

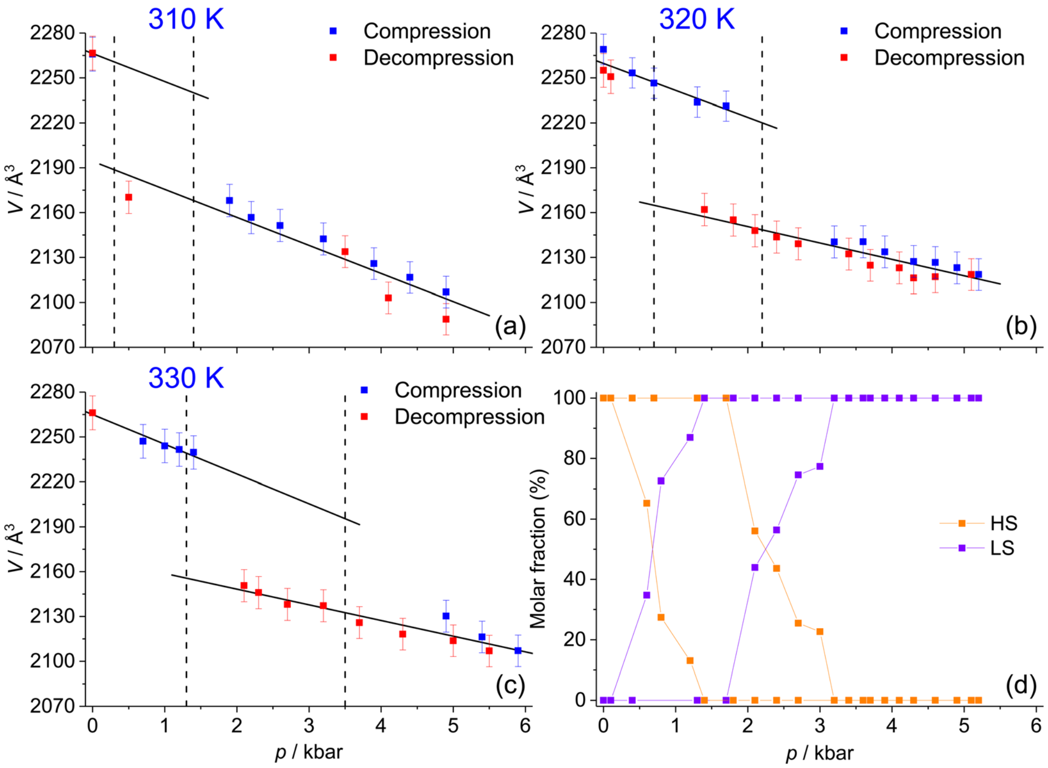

Fig. 5 The pressure dependence of the volume of [Fe(pap-5NO$_2$)$_2$] at p values where it exhibits a single phase, for the isotherms at 310 K (a), 320 K (b) and 330 K (c). Evolution of the molar fraction of each phase with pressure at 320 K (d). The p–V curves feature an isothermal hysteresis loop, where the solid lines are linear regressions, and the vertical dashed lines indicate the approximate transition pressures where a 50–50% coexistence of the HS and LS phases occurs.

compounds.[17,30,31] The volume change under isothermal conditions shows an average $\Delta V_\mathrm{T} = 75 \pm 10$ Å^3 for $Z = 4$.

Finally, applying eqn (2) to the values obtained from the combined SXRPD/XRPD experiments allows calculating the lattice entropy change, $\Delta S_\mathrm{v} = 27 \pm 3$ J kg^{-1} K^{-1}. This result aligns well with the anticipated values derived from the DSC estimations,[21] validating our approach.

3.3 High-pressure calorimetry

We measured several thermograms, dQ/dT, under isobaric conditions up to $p = 2.0$ kbar (Fig. 6). For each pressure, a sharp, dominant peak identifies the transition between the LS and HS phases. The thermograms were systematically scanned twice as the first thermal cycle resulted in a significant irreversibility (representative data in Fig. S5†), as previously observed.[21] The data shown in Fig. 6 correspond to the measurements collected during the second thermal cycle. Most likely, the irreversibility is ascribed to the sample microstructure as the volume change at the phase transition should impose a realigning torque on the crystallites during the first cycle.[32] The irreversibility is strongly suppressed on subsequent cycles and restored after each pressure change. In addition to the main peak, we observe satellite anomalies (Fig. 6). These are likely rooted in the same microstructural characteristics. When the SCO phenomenon is accompanied by strong cooperativity, as in [Fe(pap-5NO$_2$)$_2$], the ensuing phase transition is highly influenced by the anisotropy of properties and shape of the sample crystallites. This relationship has been elegantly demonstrated through optical microscopy on single-crystal samples of similar materials.[33] It is essential to note that we carefully prepared our samples without significant grinding to preserve the integrity of the spin-crossover features.[34] Therefore, it is not surprising that our precise measurements, taken at relatively slow rates, have detected these secondary anomalies. Crucially, these anomalies

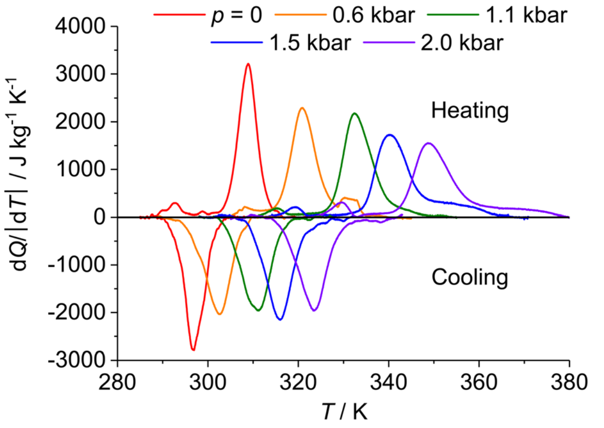

Fig. 6 Isobaric thermograms of [Fe(pap-5NO$_2$)$_2$] at different pressures, during heating (endothermal) and cooling (exothermal), upon baseline subtraction.

represent less than 5% of the total entropy content, which remains consistent across different isobaric runs, underscoring the reliability of the results. The increase in pressure plays a significant role in stabilizing the LS state, which is characterized by a smaller volume. This increase also causes the endothermal and exothermal peaks to shift to higher temperatures, in accordance with the predictions of the Clausius–Clapeyron equation and the observation of a positive ΔV_p during heating.[35]

We present the complete phase diagram for [Fe(pap-5NO$_2$)$_2$] (Fig. 7), integrating data from both high-pressure calorimetry and variable-pressure SXRPD measurements. The transition temperatures are identified at the peaks of the thermograms as well as at the even mixtures (50%) of both phases in the variable-pressure SXRPD measurements. The SCO transition shifts linearly to higher temperatures as pressure increases. Notably, the slope of temperature with respect to pressure, denoted as dT/dp, varies between the LS to HS and HS to LS transitions. In the first case, *i.e.*, isobaric heating and isothermal decompression, the value obtained is $(\mathrm{d}T/\mathrm{d}p)^{\mathrm{heat}} = 22 \pm 2$ K kbar^{-1}. Conversely, in the second case, *i.e.*, isobaric cooling and isothermal compression, the slope is $(\mathrm{d}T/\mathrm{d}p)^{\mathrm{cool}} = 10 \pm 1$ K kbar^{-1}. This disparity results in an increase in thermal hysteresis with rising applied pressure. This behavior contrasts with what is typically observed in most barocaloric materials, where thermal hysteresis tends to diminish with increasing pressure. However, the phenomenon seen in [Fe(pap-5NO$_2$)$_2$] has been documented in other studies involving SCO materials,[36,37] and can be attributed to the interplay between the effects of applied pressure, which acts on both the ligand field and the strength of the elastic interactions.[38]

3.4 Determination of the barocaloric effect

The isobaric entropy is determined using calorimetric data and the volume thermal expansion at ambient pressure ($p = p_0$). This is achieved by applying the expression:[28]

$$S(T,p) - S_0(T_0,p_0) = -\left(\frac{\partial V}{\partial T}\right)_{p=p_0} \Delta p + \int_{T_0}^{T} \frac{1}{T'} \left(c_p + \frac{\mathrm{d}Q\left(T',p\right)}{\mathrm{d}T'}\right) \mathrm{d}T'. \quad (4)$$

The first term in eqn (4) is used to calculate the pressure dependence of the heat capacity from absolute zero up to the reference temperature $T_0 = 270$ K, utilizing the Maxwell relations. A value of

$$\left(\frac{\partial V}{\partial T}\right)_{p=p_0} = (9.6 \pm 0.6) \times 10^{22}\ \mathring{\mathrm{A}}^3\ \mathrm{kg}^{-1}\ \mathrm{K}^{-1}$$

is obtained from variable-temperature ambient-pressure XRPD measurements. In the second term of eqn (2), the heat capacity, c_p, is assumed to be both temperature and pressure-independent throughout the range examined, with a constant value of 725 J kg^{-1} K^{-1}.[21] The resulting isobaric entropy curves are plotted in Fig. 8.

From the entropy curves, we compute the isothermal entropy change, ΔS_T, and the adiabatic temperature change, ΔT_{ad}, for any pressure change $\Delta p = p - p_0 \approx p$ during both compression (represented by cooling entropy curves) and decompression (represented by heating entropy curves), as follows

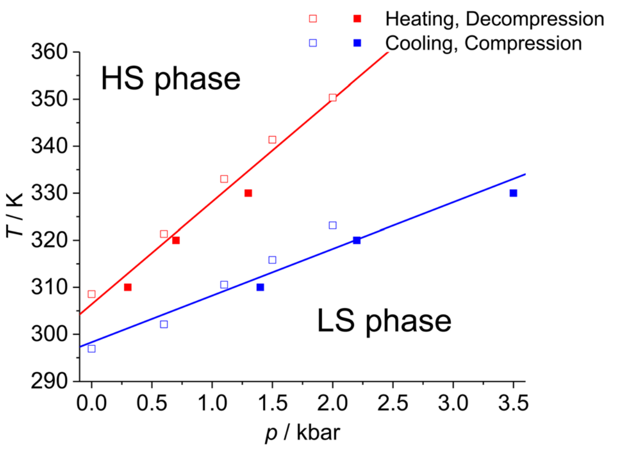

Fig. 7 Pressure–temperature phase diagram for [Fe(pap-5NO$_2$)$_2$], from high-pressure calorimetric data (open squares) and variable-pressure SXRPD data (solid squares). The solid lines are fits to the data.

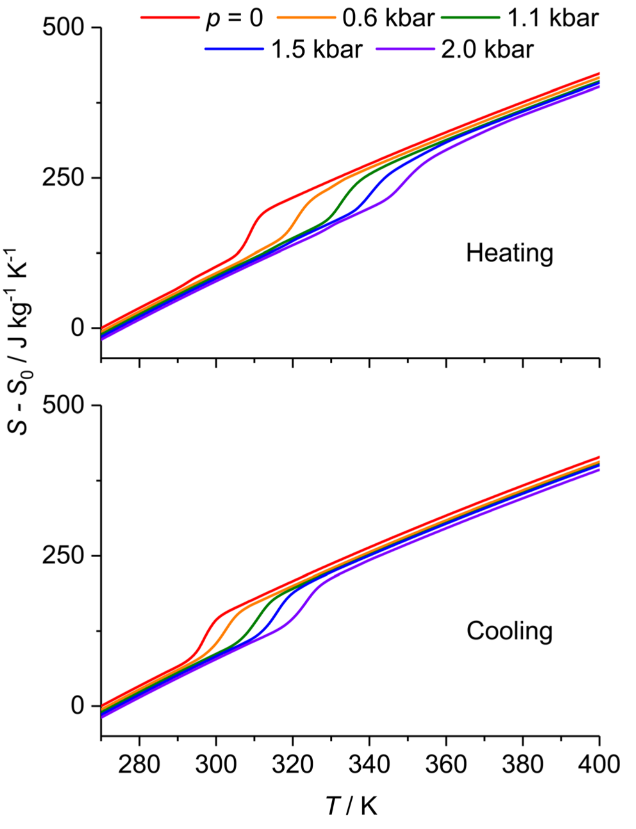

Fig. 8 Isobaric entropy of [Fe(pap-5NO$_2$)$_2$] at several pressures during heating (top) and cooling (bottom).

$$\Delta S_T = [S(T,p) - S(T,p_0)]_T \tag{5}$$

$$\Delta T_{ad} = [T(S,p) - T(S,p_0)]_S. \tag{6}$$

Notably, maxima in both $|\Delta S_T|$ and $|\Delta T_{ad}|$ are observed when the pressure change induces the SCO transition (Fig. 9). For $\Delta p = 2.0$ kbar, $|\Delta S_T|$ reaches 79 ± 4 J kg^{-1} K^{-1} on decompression and 70 ± 4 J kg^{-1} K^{-1} on compression, with the primary contribution stemming from the entropy change ΔS_{SCO}. In conjunction, for the same pressure change, $|\Delta T_{ad}|$ ranges between 20 ± 2 and 26 ± 2 K for compression and decompression, respectively. The asymmetry of the BCE arises from the difference in slope between $(dT/dp)^{heat}$ and $(dT/dp)^{cool}$.

For practical applications, evaluating the BCE under cycling conditions is crucial. The condition of reversibility is achieved only when the pressure exceeds the reversibility pressure, denoted as p_{rev}, *i.e.*, the minimum pressure necessary to overcome the thermal hysteresis, ΔT_{hyst}. Note that pressures slightly above p_{rev} are typically needed to achieve a reversible ΔT_{ad}.[6] The reversibility pressure can be estimated using the expression $p_{rev} = \Delta T_{hyst}/(dT/dp)^{cool}$, where $(dT/dp)^{cool}$ represents the slope of the phase diagram during cooling or compression. For [Fe(pap-5NO$_2$)$_2$], an estimated value of p_{rev} is approximately 1.2 kbar. Next, we compute the reversible values of the BCE figures of merit for the pressure change of $\Delta p = 2.0$ kbar (Fig. 10). The isothermal entropy change, ΔS_T^{rev}, is calculated as the overlap between ΔS_T obtained upon compression and decompression.[17,39] The adiabatic temperature change is deduced as follows,[6]

$$\Delta T_{ad}^{rev} = [T(S_{cool},p) - T(S_{heat},p_0)]_S. \tag{7}$$

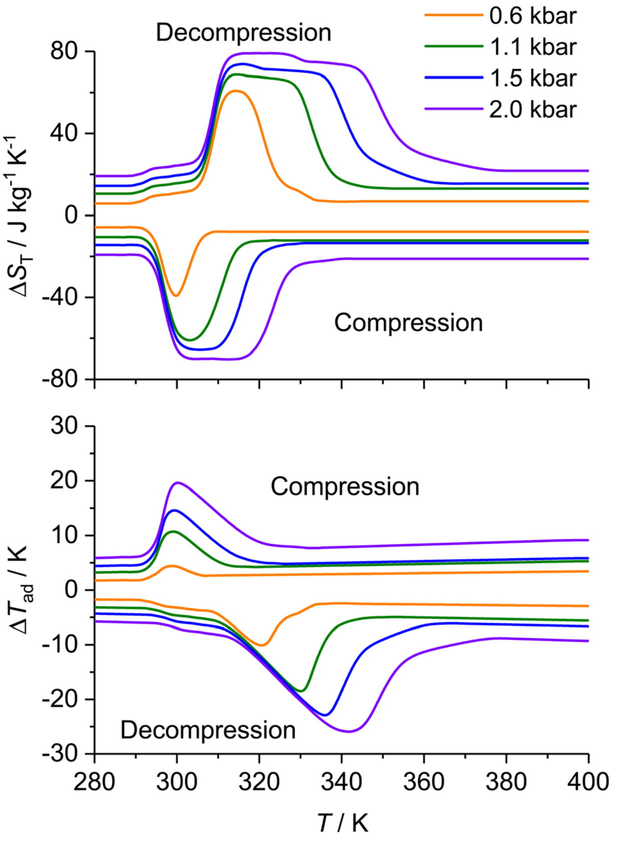

Fig. 9 Irreversible isothermal entropy change ΔS_T (top) and adiabatic temperature change ΔT_{ad} (bottom), during compression and decompression, for [Fe(pap-5NO$_2$)$_2$].

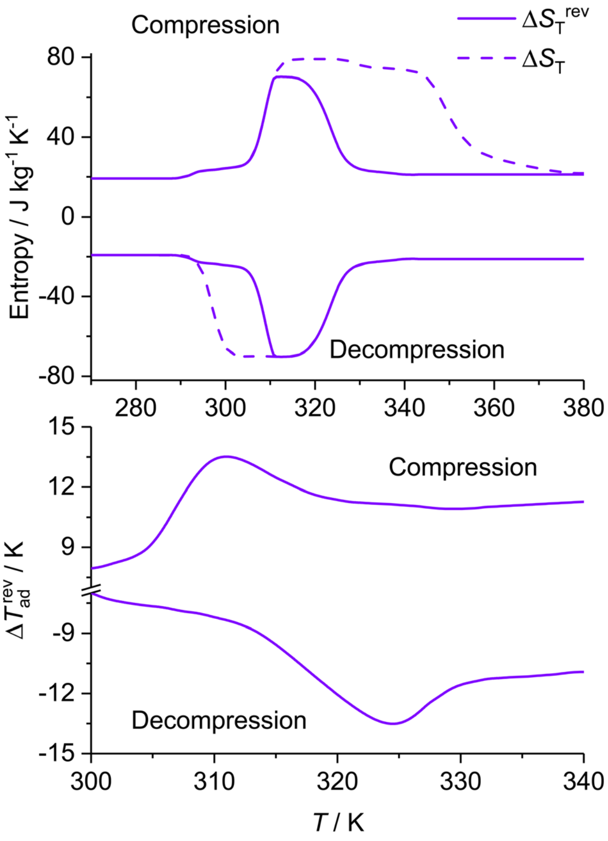

Fig. 10 Reversible isothermal entropy change (ΔS_T^{rev}, solid lines in the top panel) and reversible adiabatic temperature change (ΔT_{ad}^{rev}, bottom), for $\Delta p = 2.0$ kbar during compression and decompression. The irreversible isothermal entropy change (ΔS_T, dashed lines in the top panel) is shown for comparison.

It is noteworthy that the thermal hysteresis observed in [Fe(pap-5NO$_2$)$_2$] leads to a reduction of the BCE during cycling. This is particularly pronounced in the adiabatic temperature change, which exhibits a substantial decrease from over 20 K to a reversible change of $\Delta T_{ad}^{rev} = 14 \pm 2$ K. Conversely, the isothermal entropy change shows a minor reduction in its maximum value, decreasing from 79 to 70 J kg^{-1} K^{-1} for $\Delta p = 2.0$ kbar, as depicted in Fig. 10.

As a benchmark for evaluating the barocaloric efficiency of a material, the Coefficient of Refrigerant Performance (CRP) is often utilized. This is defined by CRP = $|\Delta S_T^{rev} \Delta T_{ad}^{rev}/W|$, where the input work W can be approximated by $W = 1/2p\Delta V$. For [Fe(pap-5NO$_2$)$_2$], the CRP yields 0.7 under a pressure change of $\Delta p = 2.0$ kbar.

Barocaloric materials exhibit a complex landscape of structural compositions. For those keen on comparing the efficiency metrics typical of various material classes, we recommend

Table 1 For selected Fe^{II} SCO compounds (top) and other cutting-edge barocaloric materials (bottom): reversible isothermal entropy change (ΔS_T^{rev}, J kg^{-1} K^{-1}); reversible adiabatic temperature change (ΔT_{ad}^{rev}, K); coefficient of refrigerant performance (CRP); temperature of the ΔS_T^{rev} maximum (T_{max}, K); applied pressure change (Δp, kbar); reference

	ΔS_T^{rev}	ΔT_{ad}^{rev}	CRP	T_{max}	Δp	Ref.
$Fe_3(bntrz)_6(tcnset)_6$	115	30	1.7	360	2.0	17
$Fe[HB(tz)_3]_2$	92	2	1.3	334	0.15	18
$[Fe(L)(NCS)_2]$	114	16	2.0	280	1.0	19
$[Fe(pz)_2(BH_3CN)_2]$	103	0	0	342	1.0	20
$[Fe(pap\text{-}5NO_2)_2]$	70	14	0.7	310	2.0	This work
AgI	60	18	1.2	395	2.5	42
NPG	510	30	1.0	330	5.7	43 and 44
C_{60}	32	10	1.3	260	1.0	45
$(C_{10}H_{21}NH_3)_2MnCl_4$	250	12	0.9	315	1.0	46
$(MnNiGe)_{0.91}(FeCoGe)_{0.09}$	19	4	0.1	290	1.0	47

exploring recent review publications.[4,40] One noteworthy addition to the field is $[Fe(pap\text{-}5NO_2)_2]$, which enhances the category of SCO materials proposed as effective barocaloric refrigerants. The values of ΔS_T and ΔT_{ad} observed in $[Fe(pap\text{-}5NO_2)_2]$ surpass those found in most SCO compounds.[12–16,41] However, this area of research has experienced rapid advancements, with very promising candidate SCO materials being reported since 2021. For a comprehensive overview, Table 1 outlines the current state-of-the-art in barocaloric SCO compounds, showcasing the calculated reversible values of key figures of merit. To enhance clarity and enable a more straightforward comparison, Table 1 also includes representatives from other families of barocaloric materials, namely superionic conductors, plastic crystals, molecular crystals, hybrid organic–inorganic perovskites and shape-memory alloys. While $[Fe(pap\text{-}5NO_2)_2]$ exhibits the lowest BCE when compared to SCO compounds with smaller thermal hysteresis,[17,19] it stands out due to its operational temperatures (T_{max}) being closer to room temperature, underscoring its potential in practical applications.

4 Conclusions

We have investigated the barocaloric properties of the $[Fe(pap\text{-}5NO_2)_2]$ Schiff-base compound, which is characterized by a first-order SCO transition occurring near room temperature. Through calorimetry and powder X-ray diffraction experiments at different pressures, we have observed giant BCE figures of merit as large as $\Delta S_T = 79$ J kg^{-1} K^{-1} and $\Delta T_{ad} = 26$ K for a pressure change of $\Delta p = 2.0$ kbar. The presence of hysteresis results in a decrease in the reversible BCE during the cycling process, with $\Delta S_T^{rev} = 70$ J kg^{-1} K^{-1} and $\Delta T_{ad}^{rev} = 14$ K at $\Delta p = 2.0$ kbar. This highlights the impact of thermal hysteresis on the barocaloric performance of this class of materials, showcasing the complexities involved in its thermal behavior.

Data availability

All data presented in this article can be retrieved from DIGITAL.CSIC at **https://doi.org/10.20350/digitalCSIC/16990**.

Author contributions

David Gracia (writing – original draft, data curation, validation, investigation, methodology, formal analysis), Vera Cuartero (methodology, data curation, validation, investigation, formal analysis, writing – review & editing), Catalin Popescu (data curation, validation), Adelais Trapali (data curation, validation), Talal Mallah (conceptualization, investigation), Marie-Laure Boillot (supervision, validation, investigation, writing – review & editing), Javier Blasco (data curation, validation, investigation), Gloria Subías (funding acquisition, supervision, data curation, validation, investigation, formal analysis, writing – review & editing), Marco Evangelisti (conceptualization, supervision, writing – review & editing, data curation, validation, investigation).

Conflicts of interest

There are no conflicts to declare.

Acknowledgements

This work was funded by MICIU/AEI/10.13039/501100011033 and ERDF/UE (PID2021-124734OB-C21, CEX2023-001286-S), Gobierno de Aragón (E11-23R, E12-23R) and Fundación IberCaja and Universidad de Zaragoza (JIUZ2023-CIE-05). D. G. acknowledges financial support from the Gobierno de Aragón through a doctoral fellowship. The authors acknowledge the Servicio General de Apoyo a la Investigación from Universidad de Zaragoza, ALBA synchrotron for granting beamtime (experiment no. 2023027379), and MSPD beamline staff for experimental and technical support.

References

1 X. Moya, S. Kar-Narayan and N. D. Mathur, *Nat. Mater.*, 2014, **13**, 439–450.
2 I. Takeuchi and K. Sandeman, *Phys. Today*, 2015, **68**, 48–54.
3 D. Boldrin, *Appl. Phys. Lett.*, 2021, **118**, 170502.
4 P. Lloveras and J. L. Tamarit, *MRS Energy Sustainability*, 2021, **8**, 3–15.
5 L. Mañosa and A. Planes, *Appl. Phys. Lett.*, 2020, **116**, 050501.
6 A. Aznar, P. Lloveras, M. Barrio, P. Negrier, A. Planes, L. Mañosa, N. D. Mathur, X. Moya and J. L. Tamarit, *J. Mater. Chem. A*, 2020, **8**, 639–647.
7 K. G. Sandeman, *APL Mater.*, 2016, **4**, 111102.
8 P. Gütlich and H. A. Goodwin, *Spin Crossover in Transition Metal Compounds I*, Springer Science & Business Media, New York City, 2004.
9 M. Nishino, Y. Singh, K. Boukheddaden and S. Miyashita, *J. Appl. Phys.*, 2021, **130**, 141102.
10 P. Guionneau, *Dalton Trans.*, 2014, **43**, 382–393.
11 P. J. von Ranke, *Appl. Phys. Lett.*, 2017, **110**, 181909.
12 P. J. von Ranke, B. P. Alho, R. M. Ribas, E. P. Nobrega, A. Caldas, V. S. R. de Sousa, M. V. Colaço, L. F. Marques, D. L. Rocco and P. O. Ribeiro, *Phys. Rev. B*, 2018, **98**, 224408.

13 P. J. von Ranke, B. P. Alho and P. O. Ribeiro, *J. Alloys Compd.*, 2018, **749**, 556–560.

14 P. J. von Ranke, B. P. Alho, E. P. Nobrega, A. Caldas, V. S. R. de Sousa, M. V. Colaço, L. F. Marques, G. M. Rocha, D. L. Rocco and P. O. Ribeiro, *J. Magn. Magn. Mater.*, 2019, **489**, 165421.

15 P. J. von Ranke, B. P. Alho, P. H. S. da Silva, R. M. Ribas, E. P. Nobrega, V. S. R. de Sousa, A. M. G. Carvalho and P. O. Ribeiro, *Phys. Status Solidi B*, 2021, **258**, 2100108.

16 S. P. Vallone, A. N. Tantillo, A. M. dos Santos, J. J. Molaison, R. Kulmaczewski, A. Chapoy, P. Ahmadi, M. A. Halcrow and K. G. Sandeman, *Adv. Mater.*, 2019, **31**, 1807334.

17 M. Romanini, Y. Wang, K. Gürpinar, G. Ornelas, P. Lloveras, Y. Zhang, W. Zheng, M. Barrio, A. Aznar, A. Gràcia-Condal, B. Emre, O. Atakol, C. Popescu, H. Zhang, Y. Long, L. Balicas, J. L. Tamarit, A. Planes, M. Shatruk and L. Mañosa, *Adv. Mater.*, 2021, **33**, 2008076.

18 J. Seo, J. D. Braun, V. M. Dev and J. A. Mason, *J. Am. Chem. Soc.*, 2022, **144**, 6493–6503.

19 M. Seredyuk, R. Li, K. Znovjyak, Z. Zhang, F. J. Valverde-Muñoz, B. Li, M. C. Muñoz, Q. Li, B. Liu, G. Levchenko and J. A. Real, *Adv. Funct. Mater.*, 2024, 2315487.

20 R. Li, Z. Zhang, Y. S. Bibik, I. A. Gural'skiy, I. V. Zatovsky, Z. Liu, Q. Li, B. Li, G. Levchenko and B. Liu, *Appl. Phys. Lett.*, 2024, **124**, 122202.

21 O. Iasco, E. Riviere, R. Guillot, M. Buron-Le Cointe, J. F. Meunier, A. Bousseksou and M. L. Boillot, *Inorg. Chem.*, 2015, **54**, 1791–1799.

22 F. Fauth, I. Peral, C. Popescu and M. Knapp, *Powder Diffr.*, 2013, **28**, S360–S370.

23 K. Yokogawa, *Jpn. J. Appl. Phys.*, 2007, **46**, 3636.

24 P. I. Dorogokupets and A. Dewaele, *High Pressure Res.*, 2007, **27**, 431.

25 C. Prescher and V. B. Prakapenka, *High Pressure Res.*, 2015, **35**, 223–230.

26 J. Rodríguez-Carvajal, *Phys. B*, 1993, **192**, 55–69.

27 D. J. David, *Anal. Chem.*, 1964, **36**, 2162–2166.

28 E. Stern-Taulats, A. Gràcia-Condal, A. Planes, P. Lloveras, M. Barrio, J. L. Tamarit, S. Pramanick, S. Majumdar and L. Mañosa, *Appl. Phys. Lett.*, 2015, **107**, 152409.

29 R. Sandrock and G. M. Schneider, *Bunsenges. Phys. Chem.*, 1983, **87**, 197–201.

30 M. Mikolasek, M. D. Manrique-Juarez, H. J. Shepherd, K. Ridier, S. Rat, V. Shalabaeva, A. C. Bas, I. E. Collings, F. Mathieu, J. Cacheux, T. Leichle, L. Nicu, W. Nicolazzi, L. Salmon, G. Molnár and A. Bousseksou, *J. Am. Chem. Soc.*, 2018, **140**, 2970–8979.

31 J. Laisney, H. J. Shepherd, L. Rechignat, G. Molnár, E. Rivière and M. L. Boillot, *Phys. Chem. Chem. Phys.*, 2018, **20**, 15951–15959.

32 S. Brooker, *Chem. Soc. Rev.*, 2015, **44**, 2880–2892.

33 H. Fourati, E. Milin, A. Slimani, G. Chastanet, Y. Abid, S. Triki and K. Boukheddaden, *Phys. Chem. Chem. Phys.*, 2018, **20**, 10142–10154.

34 M. S. Haddad, W. D. Federer, M. W. Lynch and D. N. Hendrickson, *Inorg. Chem.*, 1981, **20**, 131–139.

35 H. B. Callen, *Thermodynamics and an Introduction to Thermostatistics*, John Wiley & Sons, New Jersey, 1991.

36 E. König, G. Ritter, J. Waigel and H. A. Goodwin, *J. Chem. Phys.*, 1985, **83**, 3055–3061.

37 V. Ksenofontov, H. Spiering, A. Schreiner, G. Levchenko, H. A. Goodwin and P. Gütlich, *J. Phys. Chem. Solids*, 1999, **60**, 393–399.

38 K. Babilotte and K. Boukheddaden, *Phys. Rev. B*, 2020, **101**, 174113.

39 B. Emre, S. Yüce, E. Stern-Taulats, A. Planes, S. Fabbrici, F. Albertini and L. Mañosa, *J. Appl. Phys.*, 2013, **113**, 213905.

40 L. Cirillo, A. Greco and C. Masselli, *Therm. Sci. Eng. Prog.*, 2022, **33**, 101380.

41 P. J. von Ranke, B. P. Alho, P. H. S. da Silva, R. M. Ribas, E. P. Nobrega, V. S. R. de Sousa, M. V. Colaço, L. F. Marques, M. S. Reis, F. M. Scaldini, L. B. L. Escobar and P. O. Ribeiro, *J. Appl. Phys.*, 2020, **127**, 165104.

42 A. Aznar, P. Lloveras, M. Romanini, M. Barrio, J.-L. Tamarit, C. Cazorla, D. Errandonea, N. D. Mathur, A. Planes and X. Moya, *Nat. Commun.*, 2017, **8**, 1851.

43 P. Lloveras, A. Aznar, M. Barrio, P. Negrier, C. Popescu, A. Planes, L. Mañosa, E. Stern-Taulats, A. Avramenko and N. D. Mathur, *Nat. Commun.*, 2019, **10**, 1803.

44 B. Li, Y. Kawakita, S. Ohira-Kawamura, T. Sugahara, H. Wang, J. Wang, Y. Chen, S. I. Kawaguchi, S. Kawaguchi and K. Ohara, *Nature*, 2019, **567**, 506–510.

45 J. Li, D. Dunstan, X. Lou, A. Planes, L. Mañosa, M. Barrio, J.-L. Tamarit and P. Lloveras, *J. Mater. Chem. A*, 2020, **8**, 20354–20362.

46 J. Li, M. Barrio, D. J. Dunstan, R. Dixey, X. Lou, J. L. Tamarit, A. E. Phillips and P. Lloveras, *Adv. Funct. Mater.*, 2021, **31**, 2105154.

47 Y. Kuang, J. Qi, H. Xu, B. Yang, B. Li, Z. Li, H. Yan, Y. Zhang, C. Esling and X. Zhao, *Scr. Mater.*, 2021, **200**, 113908.